Chemical Science

ROYAL SOCIETY OF CHEMISTRY

EDGE ARTICLE

View Article Online
View Journal | View Issue

Cite this: *Chem. Sci.*, 2024, **15**, 18135

All publication charges for this article have been paid for by the Royal Society of Chemistry

Donor-modified asymmetric N/B/O multi-resonance TADF emitters for high-performance deep-blue OLEDs with the BT.2020 color gamut†

Jing Jin, ‡[a] Zhaolong He,‡[a] Di Liu, *[a] Yongqiang Mei,[c] Jiahui Wang,[c] Huihui Wan[d] and Jiuyan Li *[bc]

Received 23rd July 2024
Accepted 7th October 2024

DOI: 10.1039/d4sc04896b

rsc.li/chemical-science

Multi-resonance thermally activated delayed fluorescence (MR-TADF) materials of polycyclic heteroaromatics are attractive narrowband emitters in wide-color-gamut organic light-emitting diodes (OLEDs). However, deep-blue MR-TADF emitters with CIE coordinates fulfilling the BT.2020 standard and high efficiency still remain a significant challenge. Herein, two novel emitters **NBO-mSAF** and **NBO-pSAF** were developed by incorporating an electron donor, 10*H*-spiro[acridine-9,9′-fluorene] (SAF), at the *para*-position of the oxygen atom and the *para*-position of the boron atom in the nitrogen/boron/oxygen (N/B/O) ternary doped asymmetric MR skeleton. With appropriate electron-donating capacity and rigid spiro-structure, SAF was selected as the donor so that the long-range charge transfer triplet state (^{3}LRCT) is induced to accelerate the reverse intersystem crossing (RISC) process, while the ^{1}LRCT aligns higher than the short-range CT state (^{1}SRCT) of the N/B/O core to retain the MR characters. As a result, these optimized emitters exhibit deep-blue TADF with narrow spectra and a high RISC rate constant of 3.4×10^5 s^{-1}. In hyperfluorescence OLEDs with a TADF emitter DMAC-DPS as the sensitizer and PPF as the host, **NBO-mSAF** and **NBO-pSAF** achieved maximum external quantum efficiencies (EQE_{max}) of 26.7% and 25.2%. Interestingly, improved performance was realized in a traditional device configuration with a single bipolar host 26DCzPPy but without any sensitizer, where **NBO-mSAF** realized a higher EQE_{max} of 29.5% and CIE (0.128, 0.114), and **NBO-pSAF** exhibited an EQE_{max} of 20.5% and CIE of (0.147, 0.048). Narrow full width at half maximum (FWHM) values of 26–28 nm were achieved in both devices. Among all the deep-blue N/B/O type MR-TADF emitters with CIE$x \leq 0.15$ and CIE$y \leq 0.12$ ever reported so far, **NBO-mSAF** exhibited a highest EQE_{max} of 29.5%, which is even higher than those obtained with sensitizers, while the CIE$y = 0.048$ of the **NBO-pSAF** device is close to the standard blue (0.046) according to BT.2020, with a decent EQE of 20%.

Introduction

Organic light-emitting diodes (OLEDs) have garnered significant attention in display applications due to their multitude of advantages, encompassing lightweight design, superior color quality, expansive viewing angles, and ultra-fast response times.[1–3] OLEDs are rapidly becoming the preferred display technology for a range of consumer electronics, from smartwatches, mobile phones, and laptops to large-screen televisions and displays used in the automotive industry. Ultrahigh-definition displays must meet ever more stringent industry color standards, the most recent of which being Broadcasting Television Services 2020 (BT.2020), which are defined according to the Commission International de l'Éclairage (CIE) 1931 as (0.131, 0.046), (0.170, 0.797) and (0.708, 0.292) for blue, green and red, respectively.[4] The high performance of OLEDs relies on the efficient conversion of both electronically excited singlet (25%) and triplet (75%) excitons into photons, resulting in a high external quantum efficiency (EQE) and a small full width at half maximum (FWHM), ensuring extremely high emission color purity.[5] Thermally activated delayed fluorescence (TADF) emitters have gained widespread recognition as the most promising category of luminescent materials in OLEDs due to their ability to overcome the limitations associated with the severe triplet exciton loss observed in traditional fluorescent

[a]*Frontier Science Center for Smart Materials, College of Chemistry, Dalian University of Technology, 2 Linggong Road, Dalian, 116024, China. E-mail: liudi@dlut.edu.cn*

[b]*Shandong Laboratory of Yantai Advanced Materials and Green Manufacturing, Yantai Economic and Technological Development Zone, 300 Changjiang Road, Yantai, China. E-mail: greenjiuyanli@amgm.ac.cn*

[c]*Frontier Science Center for Smart Materials, College of Chemical Engineering, Dalian University of Technology, 2 Linggong Road, Dalian, 116024, China*

[d]*Instrumental Analysis Center, Dalian University of Technology, Dalian, 116024, China*

† Electronic supplementary information (ESI) available. See DOI: https://doi.org/10.1039/d4sc04896b

‡ These authors contributed equally to this work.

materials, as well as the high production costs associated with noble metal based phosphorescent materials.[6]

In comparison to the conventional donor–acceptor (D–A) materials, also termed as twisted intramolecular charge transfer (TICT) type TADF materials,[7,8] that are typically characterized by broad emission spectra owing to the severe structural relaxation of the excited state and thus a wide FWHM, the newly developed multiple resonance TADF (MR-TADF) materials are absolutely advantageous in terms of narrow-band character and excellent color purity. The electron-poor boron (B) and electron-rich nitrogen (N) atoms are strategically incorporated into a rigid polycyclic aromatic hydrocarbon (PAH) framework,[9,10] leveraging the anti-resonance effect between these atoms to achieve effective separation of the highest occupied molecular orbital (HOMO) and the lowest unoccupied molecular orbital (LUMO) on adjacent atoms to form short-range charge transfer (SRCT) excited states. This innovative molecular design not only facilitates suitable overlap integral of the frontier molecular orbitals (FMO) and efficient radiative transition, but also crucially restricts structural relaxation and significantly narrows the FWHM of the S_1 state (^{1}SRCT). Accordingly, the MR-TADF emitters are generally characterized by a narrow-band, perfect color purity and high photoluminescence quantum yield (PLQY), and seem to be more suitable for ultrahigh-definition displays and have become the new favorite OLED emitters in both academic and industrial fields.[1,3]

Nevertheless, most of the reported MR-TADF emitters frequently suffer from the relatively large energy difference between the lowest singlet and triplet state (ΔE_{ST}) values compared to the well-elaborated D–A type TICT-TADF emitters, resulting in the typically lower reverse intersystem crossing rate (k_{RISC}) ($<10^5$ s^{-1}) and thus severe efficiency roll-off at high luminance intensities due to significant triplet exciton annihilation issues such as triplet–triplet annihilation (TTA) and triplet polaron quenching (TPQ).[11] On the basis of the pioneering work of Hatakeyama and colleagues,[9,10] enlarging the π-conjugated structure of the MR core has become one important modification strategy for novel MR emitters. Owing to the favorable properties of the famous DABNA-1 (Fig. 1),[9] a number of MR-TADF materials were developed by constructing double or more N/B/N structures on a central benzene ring, which finally generated an enlarged π-conjugated MR core. Designed in such a way, ν-DABNA[10] (Fig. 1) demonstrated even greater advantages in performance (*e.g.* FWHM = 18 nm, $k_{RISC} = 2.0 \times 10^5$ s^{-1}, EQE_{max} = 34.4%) than the parent DABNA-1. However, the emission maximum of ν-DABNA (469 nm) was red-shifted by 10 nm from that of DABNA-1 because of the π-extension. As a result, the CIE coordinates (0.12, 0.11) deviated from the requirements defined by the National Television System Committee (0.14, 0.08).

Another typical structure modification method is to introduce an additional donor (Fig. 1) onto the N/B/N MR-skeleton to emulate the effect of traditional D–A-typed TADF emitters. By grafting a suitable electron donor, long-range charge transfer (LRCT) occurs between the MR core (acting as electron acceptor) and the donor, and the singlet LRCT excited state (^{1}LRCT)

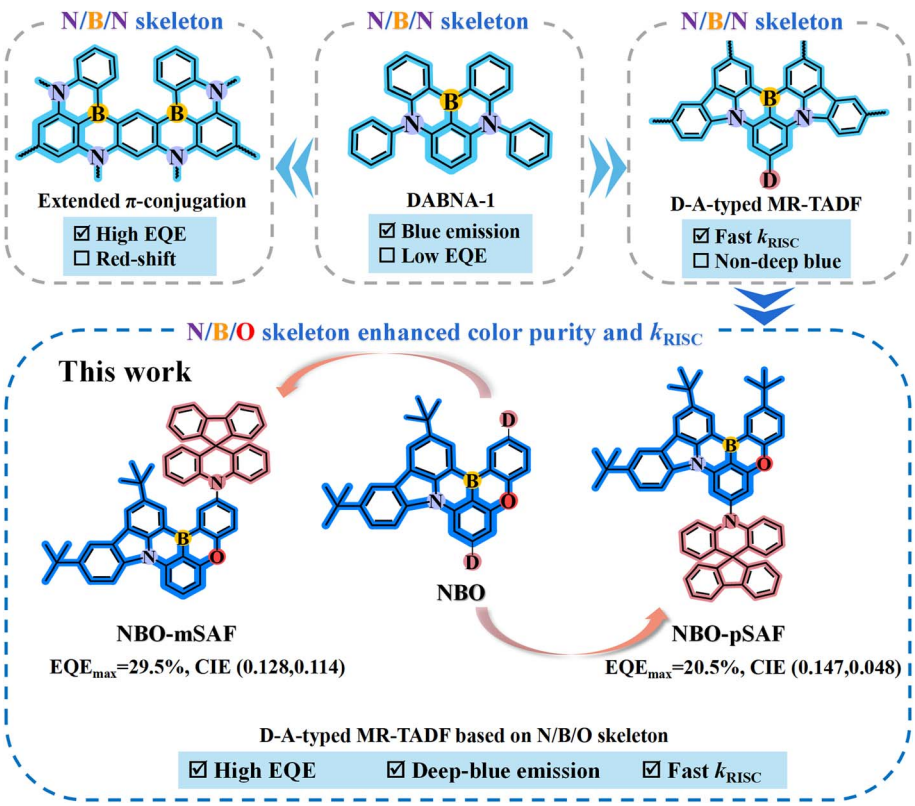

Fig. 1 Molecular design strategies and the performance summary of NBO-mSAF and NBO-pSAF.

aligns higher than the short-range CT state (^{1}SRCT) of the MR core to guarantee the stability of the MR-TADF system and to ensure narrow-band characters and perfect emitting color purity, while the appearance of the triplet LRCT state (^{3}LRCT) enriches the triplet states of the MR molecule and reduces the energy gaps between the adjacent triplet states (ΔE_{TT}) and dramatically facilitates the k_{RISC}.[12–14] Of course, the donor-modified MR-TADF derivatives definitely exhibit longer-wavelength fluorescence than the corresponding parent MR-core.[15] However, the donor strength should be carefully controlled to avoid the case that the ^{1}LRCT state falls below the ^{1}SRCT state due to the too strong donor and the original characteristic narrow-band fluorescence of the MR core gives way to the broad spectra of the ^{1}LRCT-TADF.[12,13] It is clear that both the π-extension and donor incorporation strategies on N/B/N MR-skeletons are prone to cause a bathochromic shift of the emitting light, leading to further deviation from the pure- or deep-blue range. In the recent trend, continuous research has been focused on obtaining stable MR-TADF emitters having the compatibility of a narrower FWHM and large k_{RISC} by engineering the MR effect to achieve highly stable and high color purity OLEDs.[16,17] It is established that the N/B/O asymmetrically doped PAH (Fig. 1) usually has relatively shorter wavelength emission than the similar N/B/N skeletons, which may be better candidates if deep-blue MR-TADF is desired,[18,19] especially when the rigorous BT. 2020 standard is employed.

Herein, we selected the N/B/O ternary asymmetrically doped PAH as the central MR skeleton to design two novel deep-blue MR-TADF materials, namely **NBO-mSAF** and **NBO-pSAF** (Fig. 1). 10*H*-Spiro[acridine-9,9′-fluorene] (SAF) was selected as the electron donor and was introduced for the first time at the *para*-position of the oxygen and boron atoms of the N/B/O MR-core. In comparison with the widely used acridine donor, SAF has weaker electron-donating ability. Simultaneous reduction of donor strength and acceptor strength is expected to generate relatively weak LRCT effect and make the ^{1}LRCT state locate over the intrinsic ^{1}SRCT state of the MR core to guarantee deep-blue emission.[20] More importantly, its rigid spiro structure restrains excited-state structural relaxations and vibrations and thus benefits color purity and PLQY.[20,21] Thanks to the appropriate electron-donating strength of the SAF group relative to the N/B/O MR-core and the suitably aligned ^{1}LRCT state, both **NBO-mSAF** and **NBO-pSAF** not only have the same luminescence range relative to the corresponding donor-free N/B/O MR-core but also maintain narrower FWHMs (28 nm).[22] The incorporation of the SAF donor at the periphery of the N/B/O MR nucleus played a key role in promoting the k_{RISC} and triplet exciton utilization in comparison with the corresponding donor-free N/B/O MR-core due to the contribution from the additional ^{3}LRCT state.

In the traditional structure OLEDs employing 2,6-bis(3-(9*H*-carbazol-9-yl)phenyl)pyridine (26DCzPPy) as a bipolar host, **NBO-mSAF** and **NBO-pSAF** exhibited the maximum device external quantum efficiency (EQE_{max}) of 29.5% and 20.5%, respectively, with the FWHM of 28 nm and 26 nm and CIE coordinates of (0.128, 0.114) and (0.147, 0.048), respectively. The EQE_{max} of 20.5% for **NBO-pSAF** is the highest efficiency so far for the N/B/O type deep-blue MR-TADF emitters under the BT.2020 standard (Fig. S1 and Table S1 in ESI†). Furthermore, enhanced efficiencies and dramatically suppressed efficiency roll-off were gained when a hyperfluorescence (HF) architecture with a D–A-type TADF emitter bis[4-(9,9-dimethyl-9,10-dihydroacridine)phenyl] sulfone (DMAC-DPS) as the sensitizer was utilized. The introduction of DMAC-DPS shortened the delayed fluorescence lifetime (τ_{DF}) without affecting the light color and narrow band character and significantly improved the PLQY to almost double. In addition to the remarkably improved EQE_{max} (25.2%) in the **NBO-pSAF** based HF device (*vs.* 26.7% for **NBO-mSAF**), the efficiency roll-off in both **NBO-mSAF** and **NBO-pSAF** HF devices was dramatically mitigated by means of the sensitized mechanism.

Results and discussion

Synthesis and theoretical calculation

NBO-mSAF and **NBO-pSAF** were synthesized through a palladium-catalyzed Buchwald cross-coupling reaction between the SAF fragment and the corresponding brominated MR core, NBO-mBr or NBO-pBr. The synthesis routes of intermediates and these two molecules are shown in Schemes S1 and S2,† and their structures were fully characterized by ^{1}H NMR, ^{13}C NMR and high-resolution mass spectrometry (Fig. S2–S9†).

The molecular geometry and electronic properties of the studied emitters were investigated using Density Functional Theory (DFT) and Time-Dependent DFT (TD-DFT) calculations at the M062X/def2svp level.[23] The optimized geometries of these molecules under vacuum conditions are shown in Fig. 2. The N/B/O plane and SAF donor present a highly distorted conformation, with high dihedral angles of 88.7° and 85.3° in **NBO-mSAF** and **NBO-pSAF**, respectively, similar to the general case of all acridine or acridine derivative based compounds due to the strong repulsion effect.[24,25] The HOMOs of these emitters are mainly located on the SAF due to their relatively stronger electron-donating capability than the N/B/O core, while the LUMOs are mainly located on the boron atoms and their *ortho*/*para*-carbon atoms in the N/B/O skeleton, showing a similar FMO distribution to traditional D–A type TADF emitters. **NBO-mSAF** has a slightly deeper LUMO and a shallower HOMO than **NBO-pSAF**, and thus may be expected to show a slight red-shift in fluorescence. Simultaneously, the HOMO-1 orbitals are primarily located on the nitrogen/oxygen and carbon atoms in the *ortho*/*para* positions in the N/B/O skeleton (Fig. S10†).

To clarify the emission properties, TD-DFT calculations were used to estimate the excited state energy level and analyze the natural transition orbital (NTO) (Fig. 2 and Table S2†). The results indicate that the S_1 states of both **NBO-mSAF** and **NBO-pSAF** belong to the ^{1}SRCT states, which ensures the MR characteristics of the whole molecule emission. **NBO-mSAF** and **NBO-pSAF** exhibit notable oscillator intensities (*f*) of 0.3859 and 0.3691, respectively, favoring the $S_1 \rightarrow S_0$ radiation transition. The S_2 states of **NBO-mSAF** and **NBO-pSAF** show an obvious ^{1}LRCT state feature, in which holes and electrons are distributed on the SAF and N/B/O moieties, respectively. The ^{3}LRCT is the T_4 state of **NBO-mSAF**, and is the T_5 state of **NBO-pSAF**, both of which are adjacent to their ^{1}SRCT (S_1) state. At the same time,

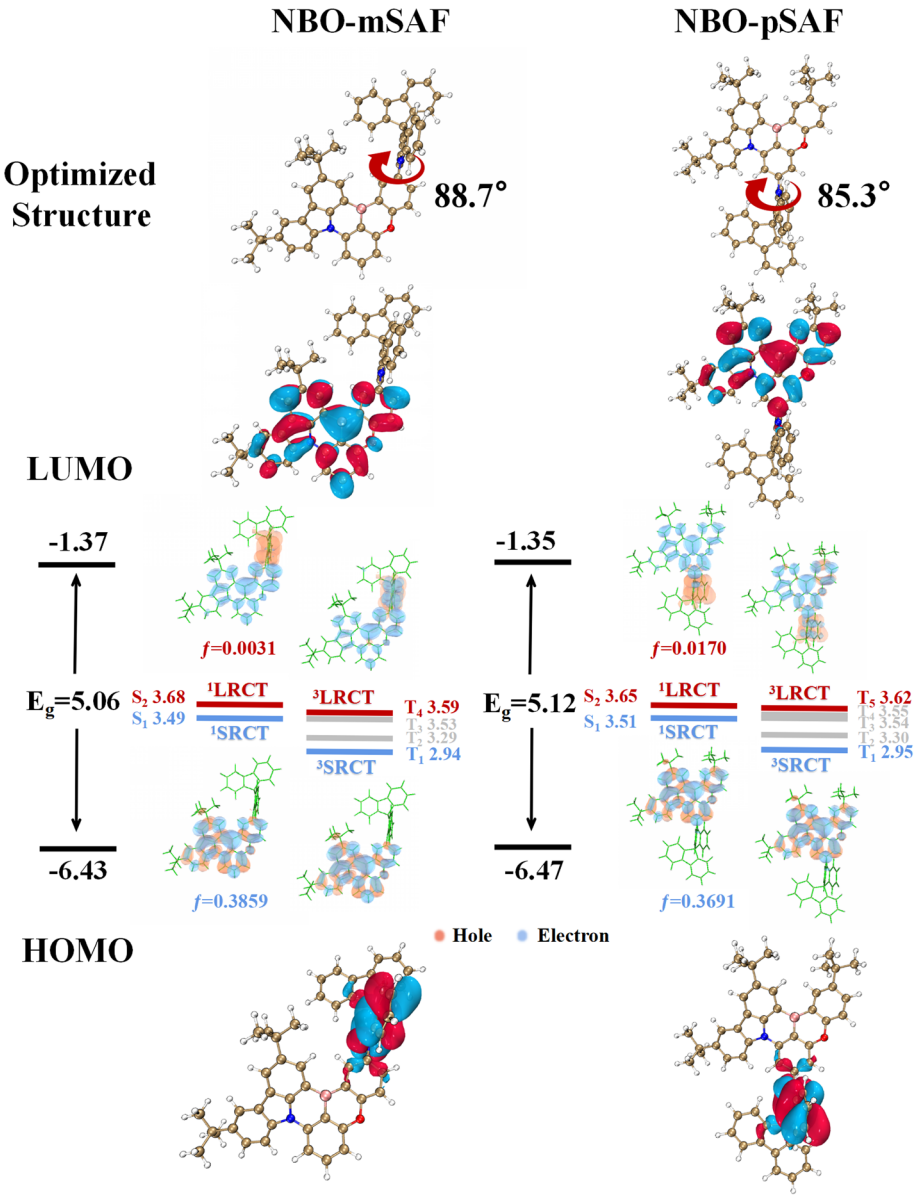

Fig. 2 Optimized geometries, HOMO and LUMO distributions, simulated energy-level diagrams and natural transition orbital (NTO) distributions for **NBO-mSAF** and **NBO-pSAF** at the M062X/def2svp level.

the energy level difference between ^{1}LRCT (S_2) and ^{1}SRCT (S_1) is small for both emitters. This means that their ^{3}LRCTs can probably act as the intermediary step to facilitate the $T_1 \rightarrow S_1$ RISC conversion, which should be supported by the possibly favorable spin orbital coupling (SOC) between the ^{3}LRCT and ^{1}SRCT (S_1) states (Table S3†). It is inferred that **NBO-mSAF** and **NBO-pSAF** may exhibit faster k_{RISC} than the parent **NBO** molecule.

Electrochemical properties

The electrochemical properties of **NBO-mSAF** and **NBO-pSAF** were investigated by cyclic voltammetry (CV) measurements (Fig. S11†). Based on the almost identical profiles of the reduction and oxidation waves for these two compounds and the theoretically observed same HOMO and LUMO distribution (Fig. 2), it would be safe to deduce that the reduction should occur on the N/B/O skeleton moiety and the oxidation corresponds to the electron loss of the SAF donor in these two molecules. The HOMO energies were determined from the onset potential (E_{ox}^{onset}) of the first oxidation wave according to the formula $E_{HOMO} = -(E_{ox}^{onset} + 4.4)$. The LUMO energies of these compounds were determined from the onset potentials of the first reduction wave (E_{red}^{onset}) according to the formula $E_{LUMO} = -(E_{red}^{onset} + 4.4)$. The resultant E_{HOMO}/E_{LUMO} values were −5.37 eV/−2.90 eV and −5.41 eV/−2.91 eV for **NBO-mSAF** and **NBO-pSAF**, respectively, and the data are summarized in Table 1. It should be noted that these HOMO and LUMO levels match well with those widely used functional materials in OLEDs,

Table 1 The experimentally determined parameters for the TADF emitters

Emitter	λ_{abs}[a] [nm]	λ_{em}[a] [nm]	FWHM[a] [nm]	E_S[b] [eV]	E_T[c] [eV]	ΔE_{ST}[c] [eV]	HOMO/LUMO[d] [eV]	E_g [eV]
NBO[22]	434	448	25	2.88	2.77	0.11	−5.40/−2.70	2.70
NBO-mSAF	440	458	28	2.78	2.56	0.22	−5.37/−2.90	2.47
NBO-pSAF	432	446	28	2.83	2.64	0.19	−5.41/−2.91	2.50

[a] Absorption and fluorescence peak wavelengths in dilute toluene solutions at room temperature. [b] Estimated from the wavelength onset of RT-FL in 2-MeTHF solution. [c] Estimated from the wavelength onset of LT-PH in 2-MeTHF solution at 77 K. $\Delta E_{ST} = E_S - E_T$. [d] Determined from electrochemical measurements.

indicating their high potential applications in optoelectronic devices.

Photophysical properties

The fundamental photophysical properties of **NBO-mSAF** and **NBO-pSAF** were investigated by means of the ultraviolet-visible (UV-vis) absorption in dilute toluene solutions (10^{-5} mol L^{-1}) and the photoluminescence (PL) spectra in dilute solutions in different polarity solvents (Fig. 3a and b). The essential photophysical parameters are compiled in Tables 1 and S4.† Absorption signals below 400 nm were attributed to the π–π* and n–π* transitions of arylamine and NBO segments, complemented by absorption bands at 440 and 432 nm for **NBO-mSAF** and **NBO-pSAF** that are characteristic of the SRCT transition within the MR segment. As predicted by the calculated results, **NBO-mSAF** exhibits a slight red-shift emission compared with **NBO-pSAF**. The fluorescence spectra of **NBO-mSAF** and **NBO-pSAF** revealed unique narrowband emissions with peaks at 458 and 446 nm and narrow FWHMs of 28 nm. Relative to the parent **NBO** that emits at 448 nm with a FWHM of 25 nm, the fluorescence of **NBO-mSAF** exhibits a 10 nm red-shift while **NBO-pSAF** has a 2 nm blue-shift, and both molecules

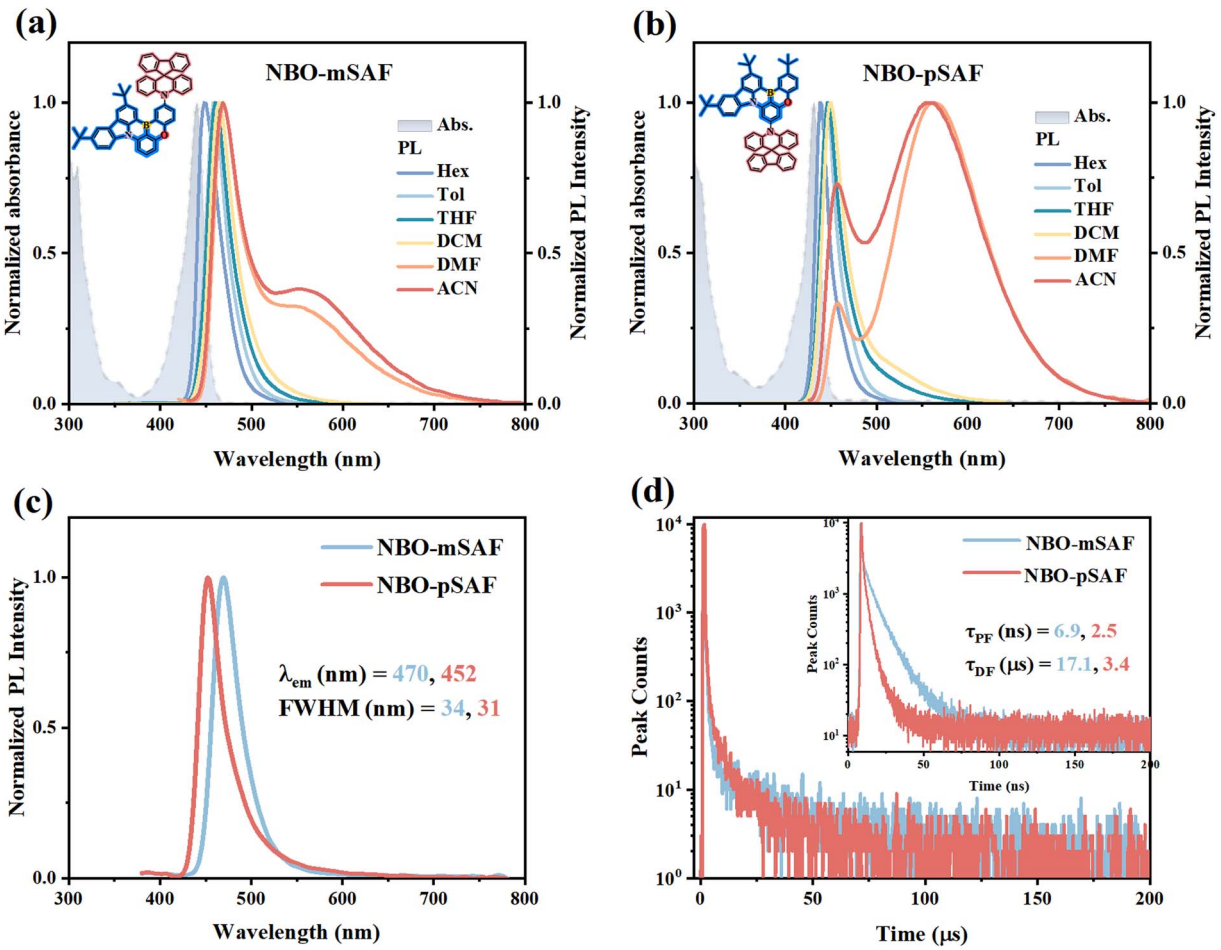

Fig. 3 Normalized UV-vis absorption in dilute toluene (10^{-5} M) solution and solvatochromic effect on photoluminescence (PL) spectra of (a) **NBO-mSAF** and (b) **NBO-pSAF**, and the normalized PL spectra (c) and transient PL decay curves (d) of **NBO-mSAF** and **NBO-pSAF** in 6 wt% doped films of 26DCzPPy.

exhibit a comparable FWHM, indicating that the introduction of the SAF donor has negligible influence on either the emitting color or the color purity.

In the solvatochromic study, the narrow-band fluorescence of both emitters exhibited tiny bathochromic effect in low polarity solvents, as illustrated in Fig. 3a, b and S12.† However, with solvent going to highly polar *N*,*N*-dimethylformamide (DMF) and acetonitrile (ACN), a new structureless and broad band appeared at near 560 nm for both emitters, which can be assigned to the fluorescence from the ^{1}LRCT states. The ^{1}LRCT states, *i.e.* the S_2 states for these two emitters, were able to be detected in DMF and ACN because they originally have rather larger transition dipole moments than the ^{1}SRCT states (S_1) and are dramatically stabilized by strong polar solvents like DMF so as to approach the ^{1}SRCT states or even drop below the ^{1}SRCT states. As a result, both the narrow-band MR fluorescence from the ^{1}SRCT state and the broad-band TICT emission from the ^{1}LRCT state can be simultaneously detected in strong polar solvents. This is essential evidence to confirm the coexistence of ^{1}SRCT and ^{1}LRCT states by finely tuning the electronic properties of the MR-core and additional donor and selecting appropriate environmental conditions. The simultaneous detection of dual fluorescence in these two emitters is consistent with the NTO calculation observation that the ^{1}SRCT and ^{1}LRCT states are closely aligned in energy levels. According to the Lippert–Mataga equation (formula (S1)–(S4)),[26] the excited dipole moments (μ_e) of the ^{1}SRCT state are calculated from the relationship between the slope of the Stokes shift ($\nu_a - \nu_f$) and the orientation polarization (f) as 10.73 and 11.36 D for **NBO-mSAF** and **NBO-pSAF**, respectively (Fig. S12 and Table S5†), which are much smaller than those of the corresponding ^{1}LRCT state (20.19 and 20.59 D). The onset points of the room temperature fluorescence (RT-FL) and low temperature (77 K) phosphorescence (LT-PH) spectra were utilized to calculate the ΔE_{ST} values, which are 0.22 eV and 0.19 eV for **NBO-mSAF** and **NBO-pSAF**, respectively (Fig. S13†). Given that the ΔE_{ST}s are sufficiently minimal, efficient RISC would be expected.

NBO-mSAF and **NBO-pSAF** were doped at 6 wt% in the 26DCzPPy host that has a large band gap and suitable T_1 energy to make films for transient PL measurements to evaluate the TADF properties. As shown in Fig. 3c, the doped films exhibit similar PL spectra profiles to those solutions, but with red-shifts of 12 nm (from 458 nm to 470 nm) accompanied by an increase of 6 nm in the FWHM (from 28 to 34 nm) for **NBO-mSAF** due to intermolecular interactions in the solid film, while **NBO-pSAF** exhibits a smaller red-shift of 4 nm (from 448 nm to 452 nm) and the FWHM is broadened by 3 nm (28 to 31 nm), indicating relatively weak intermolecular interactions in the **NBO-pSAF**:26DCzPPy film.

Through the time-correlated single photon counting (TCSPC) technique, the prompt fluorescence lifetimes (τ_{PF}) (inset of Fig. 3d) of **NBO-mSAF** and **NBO-pSAF** were determined as 6.9 ns (91.7%) and 2.5 ns (86.4%), respectively. Through the multi-channel scanning (MCS) method, in addition to the prompt fluorescence, a delayed component of each emitter was detected in the transient PL decay curve, which has an identical spectrum to the corresponding PF (Fig. S14†) and exhibits a lifetime of 17.1 μs (8.3%) for **NBO-mSAF** and 3.4 μs (13.6%) for **NBO-pSAF** (Fig. 3d and Table 2), confirming they are the delayed fluorescence (DF) of these emitters. The temperature dependent transient PL decay curves in Fig. S15† reveal that the PL intensity regularly increased with increasing temperature, especially in the short time range, confirming the TADF mechanism of the DF for these emitters. As anticipated, the introduction of donor SAF into the **NBO-mSAF** and **NBO-pSAF** resulted in a notable decrease of the τ_{DF} compared to the parent **NBO** (Table S6†), which should be favorable for effective up conversion of triplet excitons to singlet ones and inhibiting TTA and TPQ to a certain extent.

The PLQYs (Φ_{PL}) were measured as 60.0% and 52.8% for **NBO-mSAF** and **NBO-pSAF** in 26DCzPPy films (6 wt%), respectively, allowing determination of the quantum yields of PF and DF (Φ_{PF}, Φ_{DF}), and the rate constants of radiative decay (k_r), of intersystem crossing (k_{ISC}), of RISC (k_{RISC}) for each emitter (formula (S5)–(S11)). Relevant photophysical parameters are summarized in Table 2. As expected, **NBO-mSAF** and **NBO-pSAF** have larger k_{RISC}s of 6.4×10^4 s^{-1} and 3.4×10^5 s^{-1} than the parent **NBO** (1.2×10^4 s^{-1}, Table S6†). Evidently the enhanced k_{RISC}s should be mainly attributed to the introduction of the SAF donor and the ^{3}LRCT state (T_4 or T_5, Fig. 2) participates and facilitates the RISC process owing to both the tiny energy gap

Table 2 Photophysical data of **NBO-mSAF** and **NBO-pSAF** in doped films (6 wt% in 26DCzPPy and PPF) and sensitized systems (TADF sensitizer: DMAC-DPS) at room temperature[a]

		Sensitizer									
Emitter	Host	DMAC-DPS (x wt%)	Φ_{PL} [%]	Φ_{PF} [%]	Φ_{DF} [%]	τ_{PF} [ns]	τ_{DF} [μs]	k_r [10^7 s^{-1}]	k_{nr} [10^7 s^{-1}]	k_{ISC} [10^7 s^{-1}]	k_{RISC} [10^4 s^{-1}]
NBO-mSAF	26DCzPPy	—	60.0	55.0	5.0	6.9	17.1	8.0	5.3	1.2	6.4
	PPF	—	55.0	42.3	12.7	11.1	22.8	3.8	3.1	2.1	5.7
		9	96.8	61.6	35.2	17.2	17.9	3.6	0.1	2.1	8.8
		20	94.5	63.1	31.4	11.7	15.8	5.4	0.3	2.8	9.5
NBO-pSAF	26DCzPPy	—	52.8	45.6	7.2	2.5	3.4	18.3	16.4	5.5	34.1
	PPF	—	55.1	34.9	20.2	4.7	16.3	7.4	6.0	7.8	9.7
		9	84.8	42.1	42.7	9.9	18.3	4.2	0.8	5.1	11.0
		20	90.4	39.2	51.2	11.3	15.5	3.5	0.4	5.0	14.8

[a] k_r, k_{nr}, k_{ISC}, k_{RISC} represent the rate constant of radiation, non-radiation, intersystem crossing, and reverse intersystem crossing, respectively; Φ_{PL}, Φ_{PF}, Φ_{DF}, τ_{PF} and τ_{DF} represent total PLQY, quantum yield of PF, quantum yield of DF, and average lifetimes of PF and DF, respectively.

and the favorable SOC value for the ^{3}LRCT → ^{1}SRCT conversion. It is clear that **NBO-mSAF** and **NBO-pSAF** succeed in realizing an improved RISC process while preserving the ^{1}SRCT as the emitting state. The optimal equilibrium between narrowband emission and fast spin-flip highlights the potential of these two materials as efficient deep-blue emitters in OLEDs.

Electroluminescence properties

To further understand the structure–performance relationship of these MR-TADF emitters, OLEDs were fabricated with the configuration of ITO/TAPC (40 nm)/TCTA (5 nm)/26DCzPPy:*x* wt% emitters (20 nm)/TmPyPb (40 nm)/LiF (1 nm)/Al (200 nm). In these devices, ITO (indium tin oxide) and LiF/Al acted as the anode and cathode, respectively; TAPC (1,1-bis((di-4-tolylamino)phenyl)-cyclohexane) and TmPyPb (1,3,5-tri(*m*-pyridin-3-ylphenyl)benzene) were used as hole-transporting and electron-transporting layers, respectively, TCTA (4,4,4-tris(*N*-carbazolyl)triphenylamine) as the exciton-blocking layer to confine the triplet excitons within the emitting layer (EML). The bipolar transporting 26DCzPPy was selected as the host material in the EML with the expectation that its appropriately high T_1 energy (E_T = 2.71 eV) would prevent reverse energy transfer from the dopant to the host without the need for a large energy gap for energy transfer. The chemical structures of all these functional materials are shown in Fig. S16.† The device energy level diagram, the electroluminescence (EL) spectra, current density–voltage–luminance (*J*–*V*–*L*) characteristics and efficiency curves are shown in Fig. 4. The key EL performance data are summarized in Table 3.

The doping concentration was first varied (3, 6, 10 wt%) in the 26DCzPPy host to optimize the EL performance. The results (Fig. S17 and Table S7†) indicate that a doping concentration of 6 wt% led to superior performance for both **NBO-mSAF** and **NBO-pSAF**.

As shown by the inset photographs in Fig. 4c, both **NBO-mSAF** and **NBO-pSAF** devices emit deep-blue fluorescence with similar EL spectral profiles to their PL. The **NBO-mSAF** device exhibited an emission peak at 466 nm, with a FWHM of 28 nm and CIE coordinates of (0.128, 0.114), while realizing a high EQE_{max} of 29.5%. The **NBO-pSAF** device showed an EL peak of 451 nm, with a FWHM of 26 nm and CIE coordinates of (0.147, 0.048), and achieved an EQE_{max} of 20.5%. Apparently both **NBO-**

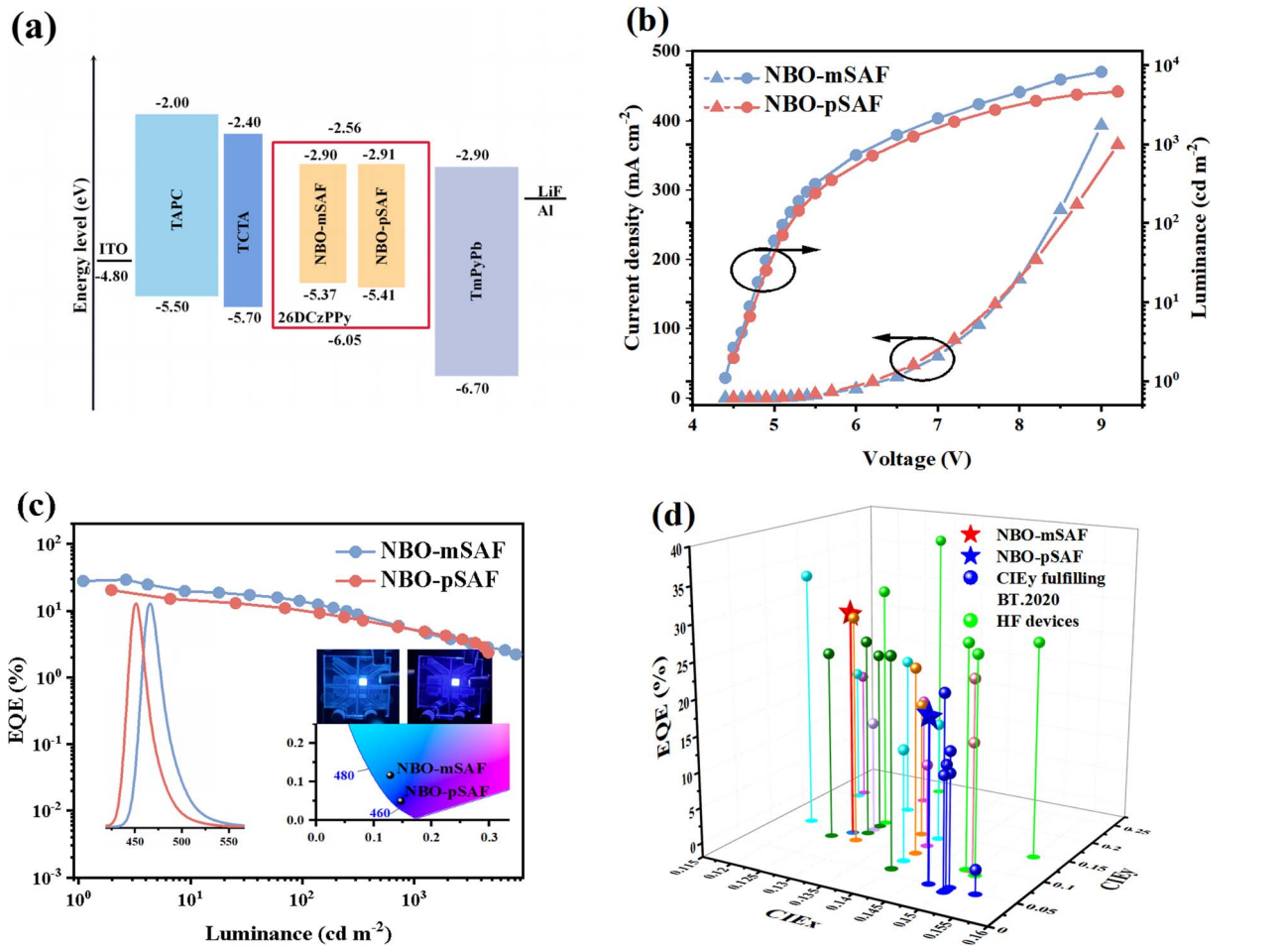

Fig. 4 Electroluminescence performance of the sensitizer-free OLEDs with 26DCzPPy as the host at a doping level of 6 wt%. (a) Device architecture and energy-level diagram, (b) *J*–*V*–*L* characteristics, (c) EQE-luminance curves (inset: EL spectra, CIE color coordinates and actual luminescence photography of **NBO-mSAF** (left) and **NBO-pSAF** (right)), and (d) comparison of the EQE_{max} and CIE coordinates of the N/B/O type blue MR-TADF emitters reported in the present study and in the literature.

Table 3 Summary of the performances of the devices (6 wt% of **NBO-mSAF** and **NBO-pSAF** in 26DCzPPy and PPF) and with different doping concentrations of the sensitizer DMAC-DPS

Emitter	Host	Sensitizer DMAC-DPS (x wt%)	V_{on}[a] [V]	λ_{EL}[b] [nm]	FWHM[c] [nm]	L_{max}[d] [cd m^{-2}]	CE_{max}[e] [cd A^{-1}]	PE_{max}[f] [lm W^{-1}]	$EQE_{max/100/1000}$[g] [%]	CIE[h] [x,y]
NBO-mSAF	26DCzPPy	—	4.4	466	28	8201	27.7	19.3	29.5/14.2/6.0	(0.128,0.114)
	PPF	—	3.4	472	34	2857	21.9	20.2	17.7/5.2/1.7	(0.120,0.180)
		9	3.2	462	34	3631	26.4	26.0	24.7/11.3/7.0	(0.142,0.127)
		20	3.0	464	38	6408	32.4	34.0	26.7/16.4/11.7	(0.137,0.154)
NBO-pSAF	26DCzPPy	—	4.5	451	26	4639	11.0	7.7	20.5/11.0/5.7	(0.147,0.048)
	PPF	—	3.8	456	32	1029	13.0	10.7	16.1/3.9/1.2	(0.142,0.087)
		9	3.4	454	33	2671	18.7	16.3	23.4/10.4/5.5	(0.146,0.089)
		20	3.2	451	38	3767	27.4	26.9	25.2/12.8/8.5	(0.154,0.117)

[a] Turn-on voltage recorded at the luminance of 1 cd m^{-2}. [b] Maximum EL wavelength. [c] FWHM of EL spectra. [d] Maximum luminance. [e] Maximum current efficiency. [f] Maximum power efficiency. [g] Efficiency at maximum and 100, 1000 cd m^{-2}. [h] EL color coordinates in the CIE 1931 chromaticity diagram recorded.

mSAF and **NBO-pSAF** devices exhibited typical device performances of the MR-TADF emitters while shifting the emission wavelength to the real deep-blue region, especially the CIEy = 0.048 for **NBO-pSAF** is almost identical to the standard blue value (0.046) under the rigorous BT.2020 standard. Furthermore, as far as we know, there have been only several examples[18,19,27–29] whose CIEy can fulfil or is close to the BT.2020 standard among all the N/B/O type blue MR-TADF emitters ever reported so far,[18,19,22,27–40] as shown in Fig. 4d and Table S1.† Evidently the EQE_{max} = 20.5% of **NBO-pSAF** is the highest efficiency so far for the N/B/O type deep-blue MR-TADF emitter with CIEy almost fulfilling the BT.2020 standard. Meanwhile, despite the slightly inferior color purity for the **NBO-mSAF** device, the EQE_{max} of 29.5% is also among the highest efficiencies for all the deep-blue N/B/O type MR-TADF emitters with CIE$x \leq 0.15$ and CIE$y \leq 0.12$ ever reported so far, which is even higher than those obtained with sensitizers (Table S1†).[30] As illustrated in Table S1,† The FWHM values of **NBO-mSAF** and **NBO-pSAF** are narrower than most of the reported FWHM values for N/B/O cored MR-TADF emitters, and are also comparable to those of MR-TADF emitters based on N/B/N structures.[12,14,27,35] Such improved color purity can be safely attributed to the high molecular rigidity induced molecular relaxation suppression in the excited state, as manifested in the photophysical behavior. It was observed that the turn on voltage (V_{on}, the voltage to deliver a brightness of 1 cd m^{-2}) was independent of the doping concentrations for both **NBO-mSAF** and **NBO-pSAF** devices, indicating the absence of a charge trapping effect in the emitting layer (Table S7†).[41] It is evident that our strategy of introducing the SAF donor into the *para*-position of either the O or B atom of the N/B/O skeleton not only significantly improved the device efficiency but also maintained excellent deep-blue color purity. However, despite the high efficiency and perfect color purity, the **NBO-mSAF** and **NBO-pSAF** devices with this traditional configuration still suffer from severe efficiency decay, with efficiency roll-off at a high brightness of 1000 cd m^{-2} over 70% from the maximum efficiencies. Therefore, it is strongly desired to improve the efficiency stability through certain device techniques.

A special device technology called hyperfluorescence (HF), proposed by Adachi *et al.*[42] and developed by Duan and coworkers,[43,44] that generally uses a TADF molecule as the sensitizer for either a traditional fluorescence dye or a narrow-band MR-TADF emitter, is characterized by high efficiency, slow efficiency roll-off and high color purity. In this approach, a high triplet energy host material, a TADF sensitizer, and a final emitter with a narrow FWHM should be considered simultaneously. Enlightened by the HF strategy, the sensitized OLEDs were fabricated by selecting bis[4-(9,9-dimethyl-9,10-dihydroacridine) phenyl]sulfone (DMAC-DPS) as the sensitizer and dibenzo[*b*,*d*] furan-2, 8-diylbis (diphenyl phosphine oxide) (PPF) as the host based on the singlet and triplet state energy requirement (Fig. 5a). Significant overlap between the fluorescence of DMAC-DPS and the absorption of the two MR-TADF emitters (Fig. S18†) guarantees efficient and forward energy transfer from the sensitizer to the MR-TADF emitters. The HF OLEDs have a configuration of ITO/HAT-CN (5 nm)/TAPC (20 nm)/TCTA (5 nm)/mCP (5 nm)/PPF:x wt% DMAC-DPS:1 wt% emitters (20 nm)/PPF (5 nm)/TmPyPb (40 nm)/LiF (1 nm)/Al (200 nm). The electron-transporting PPF was selected as the host in the EML with the expectation that its higher T_1 energy than the dopants is able to prevent reverse energy transfer from the dopant and TADF sensitizer to the host. TCTA, mCP (1,3-bis(*N*-carbazolyl)benzene) and PPF with sufficiently high triplet energies were used as exciton-blocking layers to confine the triplet excitons within the EML. The chemical structure of each functional layer material and the device energy level diagram are shown in Fig. S15† and 5b.

In general, a fast Förster resonance energy transfer (FRET) from S_1 of the TADF sensitizer to the S_1 of the fluorescent emitter is crucial to activating the HF system. By deliberately employing a low dopant concentration of 1 wt% for the N/B/O terminal emitter, the Dexter energy transfer (DET) from the triplet excitons of the sensitizer to the MR emitter was intentionally suppressed, thereby favoring the dominance of FRET as the primary mechanism for the energy transfer from PPF to both the DMAC-DPS sensitizer and MR emitter. However, the doping content of the DMAC-DPS sensitizer was controlled

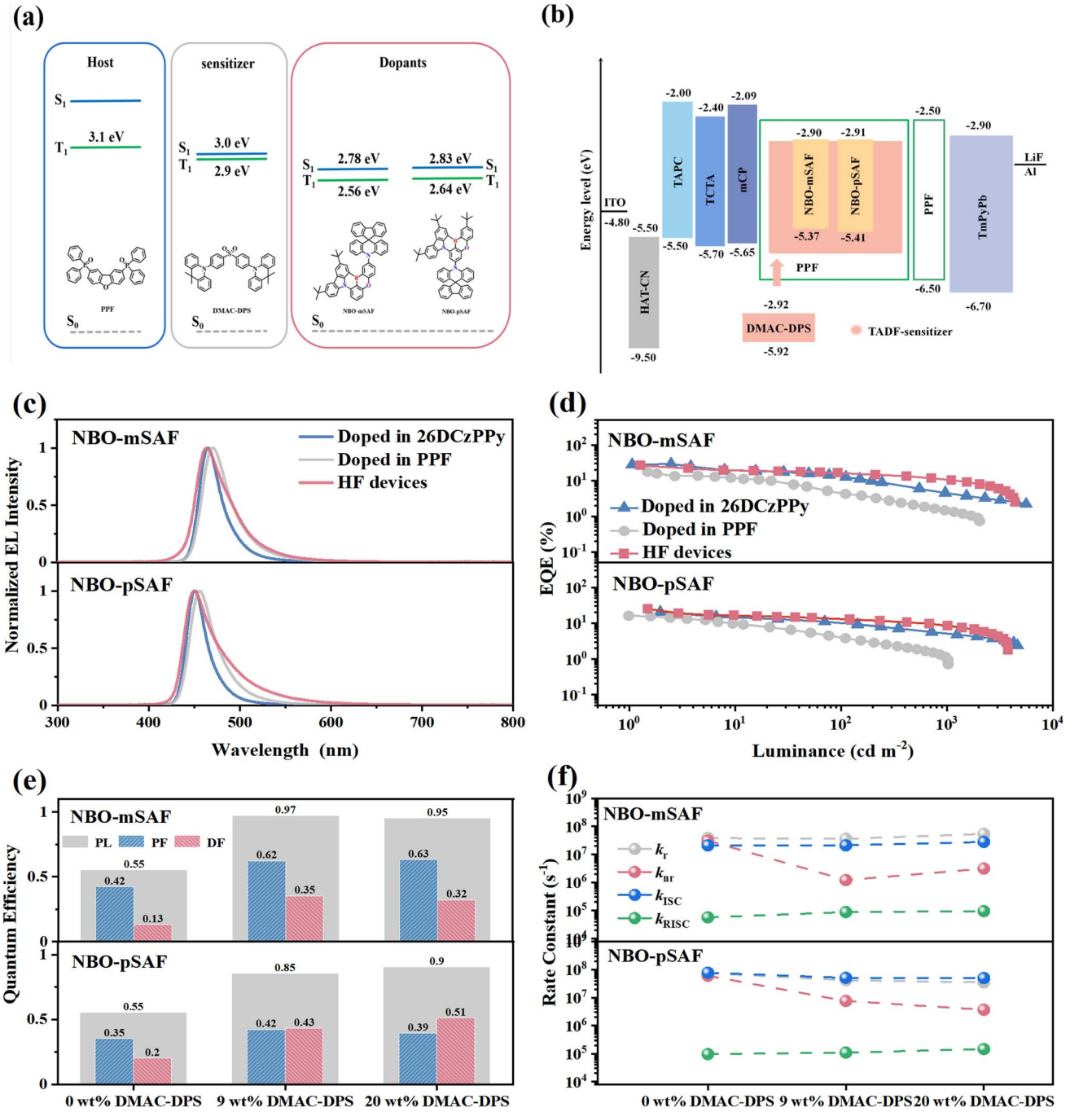

Fig. 5 Performance summary of the HF OLEDs with DMAC-DPS as the sensitizer. (a) Energy level diagram of each material in the EML layer and (b) the device structure and the energy level diagram of each functional material of the HF devices; (c) contrast of EL peaks and (d) EQEs of emitters in sensitizer-free devices of 26DCzPPy and PPF and in HF devices with DMAC-DPS (20 wt%). (e) Quantum yields and (f) the key rate constants of the sensitizer at different doping concentrations (sensitizer: DMAC-DPS) of **NBO-mSAF** and **NBO-pSAF**.

relatively high at 9% or 20% in the EML to enable the Dexter energy transfer from the PPF host to the DMAC-DPS sensitizer. In such a way, the generated triplet excitons of DMAC-DPS can be converted, in the case of the forbidden Dexter energy from DMAC-DPS to the MR emitter, into its own singlet exciton through efficient RISC based on its intrinsic TADF nature (Fig. S19†). In a similar way, it was observed that a doping level of 6 wt% for **NBO-mSAF** and **NBO-pSAF** was the favorite concentration for optimized performance when they were doped into PPF in sensitizer-free OLEDs (Fig. S20 and Table S8†). Furthermore, in the HF OLEDs with the EML having the configuration of PPF:DMAC-DPS (*x* wt%):MR emitter (1 wt%), it was observed that a doping content of 20 wt% for the DMAC-DPS sensitizer in the EML led to better performance than 9 wt% (Fig. S21†). The key device parameters are summarized in Table 3.

As shown in Fig. 5c, the HF devices exhibited emission originating from the **NBO-mSAF** and **NBO-pSAF** emitters without the residual emission from the sensitizer or host, indicating effective energy transfer sensitizing processes. As illustrated in Fig. 5d, HF devices exhibit minimal efficiency roll-offs while maintaining high efficiency in comparison to those of unsensitized devices. The EQE_{max} of the **NBO-mSAF**-based HF device is 26.7%, which is slightly lower than that in the 26DCzPPy host. However, the efficiency roll-off was greatly reduced from 79.7% (in 26DCzPPy) to 56.2% (HF) at 1000 cd m^{-2}. This improvement in efficiency stability is more pronounced in the PPF host, with a reduction from 90.4% (PPF) to 56.2% at 1000 cd m^{-2}. Furthermore, **NBO-pSAF** realized a significant EQE_{max} increase to 25.2% in the HF device and a remarkably suppressed efficiency roll-off of 66.3% at 1000 cd m^{-2}, in contrast to the values of 72.1% in 26DCzPPy and 92.5% in PPF.

The comparable or improved efficiencies and greatly suppressed efficiency roll-offs in the TADF-sensitized HF devices with the PPF:DMAC-DPS:MR emitter emitting layer configuration indicate the effective mitigation of triplet-related quenching facilitated by the sensitizer. This is evidenced by the change in the relevant photophysical parameters measured in the corresponding doping film (Table 2). In the two-component host-dopant films with 26DCzPPy or PPF as the host, both **NBO-mSAF** and **NBO-pSAF** exhibit almost comparable Φ_{PL}s (60.0% *vs.* 55.0% for **NBO-mSAF**, 52.8% *vs.* 55.1% for **NBO-pSAF**), although both the k_r and k_{nr} of 26DCzPPy are simultaneously superior to those of PPF (Table 2) for each TADF emitter. This is probably because the larger molecular dipole moment of the 26DCzPPy host (bipolar) than that of PPF (single polar) is more favorable for both the radiative and non-radiative transitions of the dopant molecules, and finally leads to comparable PLQYs in these different hosts, as illustrated by the formula (S8)–(S10) in the ESI.† Interestingly the introduction of the DMAC-DPS sensitizer greatly increases the Φ_{PL} of the doped films. For **NBO-mSAF** and **NBO-pSAF**, the PLQYs increase from 55.0% to 94.5% and 90.4% respectively (Fig. 5e). As shown in Fig. 5f, the non-radiative rate constant (k_{nr}) reduced by an order of magnitude (from 3.1×10^7 s^{-1} and 6.0×10^7 s^{-1} to 3.0×10^6 s^{-1} and 4.0×10^6 s^{-1} for **NBO-mSAF** and **NBO-pSAF**, respectively), with the presence of the DMAC-DPS sensitizer, which well accounts for the substantial increase of PLQYs of the two MR-TADF emitters and thus the obvious increase of their EQEs. Furthermore, the k_{RISC} has increased to a certain extent (from 5.7×10^4 s^{-1} and 9.7×10^4 s^{-1} to 9.5×10^4 s^{-1} and 1.5×10^5 s^{-1} for **NBO-mSAF** and **NBO-pSAF**, respectively). This is reflected in the correspondingly reduced τ_{DF} (from 22.8 μs and 16.3 μs to 15.8 μs and 15.5 μs for **NBO-mSAF** and **NBO-pSAF**, respectively) (Fig. S22† and Table 2). Such enhanced RISC in the HF OLEDs greatly improves the up-conversion and utilization rates of triplet excitons in the EML, and consequently improves the device efficiency and suppresses the efficiency roll-off.

Conclusion

Two novel MR-TADF emitters **NBO-mSAF** and **NBO-pSAF** were developed by decorating a N/B/O ternary doped asymmetrical MR skeleton with a highly rigid electron donor 10*H*-spiro[acridine-9,9′-fluorene] (SAF) at the *para*-position of the oxygen atom and the *para*-position of the boron atom. Due to the appropriate donor strength of the SAF group relative to the MR core as the acceptor, the long-range charge transfer singlet state (^{1}LRCT) was located over the short-range charge transfer singlet state (^{1}SRCT) of the N/B/O core, so that the intrinsic narrow-band emitting feature of MR-TADF was kept for both emitters. In addition, the presence of the ^{3}LRCT state compressed the triplet states and thus facilitated the RISC process. As a result, the rate constants of RISC (k_{RISC}) of **NBO-mSAF** and **NBO-pSAF** were increased by 5–10 times relative to the parent **NBO** molecule, *e.g.* to 3.4×10^5 s^{-1} for **NBO-pSAF**. In the traditional OLEDs with 26DCzPPy as the host, **NBO-pSAF** realized an EQE_{max} of 20.5% with a CIE of (0.147, 0.048) and FWHM of 26 nm, which is the highest efficiency for a N/B/O type deep-blue MR-TADF emitter with CIE*y* close to that of the BT.2020 standard (0.046). Meanwhile, despite the slightly inferior CIE coordinates of (0.128, 0.114), the EQE_{max} of 29.5% for the **NBO-mSAF** device is also among the highest efficiencies for all the deep-blue N/B/O type MR-TADF emitters with CIE$x \leq 0.15$ and CIE$y \leq 0.12$ ever reported so far, which is even higher than those obtained with sensitizers. In order to improve the efficiency stability, hyperfluorescence (HF) OLEDs were also fabricated with the emitting layer of the PPF:DMAC-DPS:MR emitter. Satisfactory EQEs of 26.7% and 25.2% were achieved for **NBO-mSAF** and **NBO-pSAF**, respectively. More importantly, the efficiency roll-off of these HF devices was dramatically suppressed owing to the reduced delay fluorescence lifetime and increased PLQY of the MR-TADF emitters with the presence of the sensitizer DMAC-DPS. As far as we know, among all the N/B/O type deep-blue MR emitters, **NBO-mSAF** is also the first example with an additional donor (SAF in the present case) incorporated into the *para*-site of the oxygen atom of the MR core, which in turn exhibited an excellent EQE_{max} of 29.5%. Furthermore, the EQE_{max} of 20.5% for **NBO-pSAF** is the highest efficiency recorded so far for N/B/O type deep-blue MR-TADF emitters with CIE*y* approaching that of the BT.2020 standard.

Data availability

All the necessary data to support the findings of this study can be found within the main text and ESI.†

Author contributions

Jing Jin: device preparation, characterization, data curation, investigation, writing – original draft. Zhaolong He: synthesis and methodology. Di Liu: investigation, project administration, resources, supervision. Yongqiang Mei: methodology and investigation. Jiahui Wang: software and formal analysis. Huihui Wang: methodology and data curation. Jiuyan Li: funding acquisition, investigation, supervision, writing – review and editing.

Conflicts of interest

There are no conflicts of interests to declare.

Acknowledgements

We thank the National Natural Science Foundation of China (22078051 and 22478063), the Fundamental Research Funds for the Central Universities (DUT22LAB610) and the Open Fund of the Key Laboratory of Advanced Display and System Applications, Ministry of Education, Shanghai University (OF202401) for financial support of this work.

References

1 Y. X. Hu, J. Miao, T. Hua, Z. Huang, Y. Qi, Y. Zou, Y. Qiu, H. Xia, H. Liu, X. Cao and C. Yang, *Nat. Photonics*, 2022, **16**, 803–810.
2 T. Huang, Q. Wang, H. Zhang, Y. Zhang, G. Zhan, D. Zhang and L. Duan, *Nat. Photonics*, 2024, **18**, 516–523.
3 M. Mamada, A. Aoyama, R. Uchida, J. Ochi, S. Oda, Y. Kondo, M. Kondo and T. Hatakeyama, *Adv. Mater.*, 2024, 2402905.
4 R. Zhu, Z. Luo, H. Chen, Y. Dong and S.-T. Wu, *Opt. Express*, 2015, **23**, 23680.
5 H. Uoyama, K. Goushi, K. Shizu, H. Nomura and C. Adachi, *Nature*, 2012, **492**, 234–238.
6 X. Cai and S. Su, *Adv. Funct. Mater.*, 2018, **28**, 1802558.
7 D. Karthik, Y. H. Jung, H. Lee, S. Hwang, B. Seo, J. Kim, C. W. Han and J. H. Kwon, *Adv. Mater.*, 2021, **33**, 2007724.
8 Y. Shi, H. Ma, Z. Sun, W. Zhao, G. Sun and Q. Peng, *Angew. Chem.*, 2022, **134**, e202213463.
9 T. Hatakeyama, K. Shiren, K. Nakajima, S. Nomura, S. Nakatsuka, K. Kinoshita, J. Ni, Y. Ono and T. Ikuta, *Adv. Mater.*, 2016, **28**, 2777–2781.
10 Y. Kondo, K. Yoshiura, S. Kitera, H. Nishi, S. Oda, H. Gotoh, Y. Sasada, M. Yanai and T. Hatakeyama, *Nat. Photonics*, 2019, **13**, 678–682.
11 H. Lim, S. Woo, Y. H. Ha, Y. Kim and J. Kim, *Adv. Mater.*, 2022, **34**, 2100161.
12 Z. Huang, H. Xie, J. Miao, Y. Wei, Y. Zou, T. Hua, X. Cao and C. Yang, *J. Am. Chem. Soc.*, 2023, **145**, 12550–12560.
13 Q. Wu, J. Li, D. Liu, Y. Mei, B. Liu, J. Wang, M. Xu and Y. Li, *Dyes Pigm.*, 2023, **217**, 111421.
14 S. Chen, Y. Wang, J. Lin, R. Tian, S. Li, Y. Man, S. Chen, J. Zhang, C. Duan, C. Han and H. Xu, *Chem. Eng. J.*, 2024, **489**, 151517.
15 F. Liu, Z. Cheng, L. Wan, Z. Feng, H. Liu, H. Jin, L. Gao, P. Lu and W. Yang, *Small*, 2022, **18**, 2106462.
16 Z. Ye, H. Wu, Y. Xu, T. Hua, G. Chen, Z. Chen, X. Yin, M. Huang, K. Xu, X. Song, Z. Huang, X. Lv, J. Miao, X. Cao and C. Yang, *Adv. Mater.*, 2024, **36**, 2308314.
17 L. Wu, X. Mu, D. Liu, W. Li, D. Li, J. Zhang, C. Liu, T. Feng, Y. Wu, J. Li, S.-J. Su and Z. Ge, *Angew. Chem., Int. Ed.*, 2024, e202409580.
18 I. S. Park, M. Yang, H. Shibata, N. Amanokura and T. Yasuda, *Adv. Mater.*, 2022, **34**, 2107951.
19 I. S. Park, H. Min and T. Yasuda, *Angew. Chem., Int. Ed.*, 2022, **61**, e202205684.
20 H. Lim, H. J. Cheon, S. Woo, S. Kwon, Y. Kim and J. Kim, *Adv. Mater.*, 2020, **32**, 2004083.
21 Y. H. Lee, W. Lee, T. Lee, J. Jung, S. Yoo and M. H. Lee, *Chem. Eng. J.*, 2023, **452**, 139387.
22 G. Liu, H. Sasabe, K. Kumada, H. Arai and J. Kido, *Chem.–Eur. J.*, 2022, **28**, e202201605.
23 T. Lu and F. Chen, *J. Comput. Chem.*, 2012, **33**, 580–592.
24 B. Chen, H. Liu, J. Yang, M. Ahmadi, Q. Chen, N. Yin, S. Zhang, M. Xiao, H. Zhang, L. Xu and P. Chen, *Adv. Funct. Mater.*, 2024, 2402522.
25 H. Liu, Y. Fu, J. Chen, B. Z. Tang and Z. Zhao, *Adv. Mater.*, 2023, **35**, 2212237.
26 Y. Yin, X. Lai, Q. Ma, H. Ma, W. Zhu, J. Y. Lee and Y. Wang, *Adv. Mater.*, 2024, **36**, 2313656.
27 J. Park, J. Lim, J. H. Lee, B. Jang, J. H. Han, S. S. Yoon and J. Y. Lee, *ACS Appl. Mater. Interfaces*, 2021, **13**, 45798–45805.
28 C.-Y. Chan, S. Madayanad Suresh, Y.-T. Lee, Y. Tsuchiya, T. Matulaitis, D. Hall, A. M. Z. Slawin, S. Warriner, D. Beljonne, Y. Olivier, C. Adachi and E. Zysman-Colman, *Chem. Commun.*, 2022, **58**, 9377–9380.
29 J. Jin, M. Chen, H. Jiang, B. Zhang, Z. Xie and W.-Y. Wong, *ACS Mater. Lett.*, 2024, 3246–3253.
30 X. Huang, Y. Xu, J. Miao, Y.-Y. Jing, S. Wang, Z. Ye, Z. Huang, X. Cao and C. Yang, *J. Mater. Chem. C*, 2023, **11**, 11885–11894.
31 Y. Xu, J. Han, N. Li, Z. Huang, J. Miao and C. Yang, *J. Mater. Chem. C*, 2023, **11**, 13733–13739.
32 H. Tanaka, S. Oda, G. Ricci, H. Gotoh, K. Tabata, R. Kawasumi, D. Beljonne, Y. Olivier and T. Hatakeyama, *Angew. Chem., Int. Ed.*, 2021, **60**, 17910–17914.
33 X. Luo, H. Ni, A. Lv, X. Yao, H. Ma and Y. Zheng, *Adv. Opt. Mater.*, 2022, **10**, 2200504.
34 J. Liu, L. Chen, X. Wang, Q. Yang, L. Zhao, C. Tong, S. Wang, S. Shao and L. Wang, *Macromol. Rapid Commun.*, 2022, **43**, 2200079.
35 J. Han, Z. Huang, X. Lv, J. Miao, Y. Qiu, X. Cao and C. Yang, *Adv. Opt. Mater.*, 2022, **10**, 2102092.
36 Z. Yan, L. Yuan, Y. Zhang, M. Mao, X. Liao, H. Ni, Z. Wang, Z. An, Y. Zheng and J. Zuo, *Adv. Mater.*, 2022, **34**, 2204253.
37 J. Jin, C. Duan, H. Jiang, P. Tao, H. Xu and W. Wong, *Angew. Chem., Int. Ed.*, 2023, **62**, e202218947.
38 K. R. Naveen, J. H. Oh, H. S. Lee and J. H. Kwon, *Angew. Chem., Int. Ed.*, 2023, **62**, e202306768.
39 X. He, J. Lou, B. Li, X. Dong, F. Zhong, W. Liu, X. Feng, D. Yang, D. Ma, Z. Zhao, Z. Wang and B. Z. Tang, *Adv. Mater.*, 2024, **36**, 2310417.
40 J. Hu, Y. Wei, X. Wang, X. Liang, X. Liao, L. Yuan, H. Ni and Y. Zheng, *Adv. Opt. Mater.*, 2024, **12**, 2302987.
41 M. Tanaka, C.-Y. Chan, H. Nakanotani and C. Adachi, *Nat. Commun.*, 2024, **15**, 5950.
42 Q. Zhang, B. Li, S. Huang, H. Nomura, H. Tanaka and C. Adachi, *Nat. Photonics*, 2014, **8**, 326–332.
43 X. Song, D. Zhang, Y. Lu, C. Yin and L. Duan, *Adv. Mater.*, 2019, **31**, 1901923.
44 C. Yin, Y. Zhang, T. Huang, Z. Liu, L. Duan and D. Zhang, *Sci. Adv.*, 2022, **8**, eabp9203.